

Trace Coherence: a new operator for polarimetric and interferometric SAR images

Armando Marino, *Member, IEEE*

ABSTRACT

Quadratic forms play an important role in the development of several Polarimetric and Interferometric Synthetic Aperture Radar (Pol-InSAR) methodologies, which are very powerful tools for Earth Observation.

This work investigates integrals of Pol-InSAR operators based on quadratic forms, with special interest for the Pol-InSAR coherence. A new operator is introduced, namely Trace Coherence, that provides an approximation for the center of mass of the Coherence Region (CoRe). The latter is the locus of points on the polar plot containing all the possible coherence values. Such center of mass can be calculated as the integral of Pol-InSAR coherences over the scattering mechanisms. The Trace Coherence provides a synthetic information regarding the partial target as one single entity. Therefore, it provides a representation, which is not dependent on the selection of one specific polarization channel. It may find application in change detection (e.g. Coherent Change Detection and differential DEM), classification (e.g. building structure parameters) and modeling (e.g. for the retrieval of forest height).

Armando Marino is with the Open University, Engineering and Innovation, Milton Keynes, United Kingdom (e-mail: armando.marino@open.ac.uk).

In calculating the integral of the Pol-InSAR coherences, an approximate Trace Coherence expression is derived and shown to improve the calculation speed by several orders of magnitude.

The Trace Coherence approximation is investigated using Monte Carlo simulations and validated ESA (DLR) L-band quad-polarimetric data acquired during the AGRISAR 2006 campaign. The result of the analysis using simulated and real data is that the average error in approximating the integral of the Coherence Region is 0.025 in magnitude and 3 degree in phase (in scenarios with sufficiently high coherence).

I. INTRODUCTION

Synthetic Aperture Radars (SAR) are powerful sensors able to acquire high resolution images of scene reflectivity at microwave frequencies [1]. Such products are complementary to optical images and have the advantage of measuring with almost any weather conditions and at night time. Also, microwaves can penetrate some class of targets providing information on the internal target structure [2]. For those reasons, SAR has been largely used for stationary target detection and recognition, multi-pass target change detection and retrieval of biophysical parameters (specially related to vegetation). Finally, the use of multiple polarimetric channels (i.e. 2 or 3 channels) or multiple flight passes (i.e. baselines) increases substantially the amount of observables allowing the development of more powerful methodologies [3], [4]. The combination of polarization and interferometry is often referred to as Pol-InSAR [5], [6]. In the last decades a large variety of PolSAR and Pol-InSAR methodologies were proposed. A very short list of applications are retrieval of parameters [7], [8], [9], detection/classification [10], [11], [12], [13] and change detection [14], [15], [16], [17].

In the following, a very brief introduction to Pol-InSAR is provided with the purpose of

16 presenting the mathematical formalism exploited in the rest of the paper.

17 A single target has a fixed polarization in time/space and we can characterize it using a
 18 scattering (Sinclair) matrix or equivalently a scattering vector \underline{k} [3]. In a linear polarization
 19 basis, the scattering vector is typically given as $\underline{k} = [HH, HV, VV]^T$, where HH, HV, and
 20 VV are the complex radar returns gathered by the radar. It is possible to define a projection
 21 vector as a normalized vector $\underline{\omega} = \frac{\underline{k}}{\|\underline{k}\|}$. $\underline{\omega}$ is by the community often referred to as Scattering
 22 Mechanism (SM), however the concept of SM should be referred to a physical target while
 23 $\underline{\omega}$ is an entity that we use to focus or filter out a specific SM. Typically, the target observed
 24 by a SAR system is not a single SM, but a combination of different targets which we refer
 25 to as partial targets. In order to characterize a partial target the single scattering matrix
 26 is not sufficient, since the target is a stochastic process and the second order statistics are
 27 required. In this context, the target covariance matrix can be estimated: $T = \langle \underline{k} \underline{k}^{*T} \rangle$, where
 28 $*$ stands for conjugate, superscript T for transpose and $\langle . \rangle$ is the finite averaging operator
 29 [3]. Please note, in this paper we will not differentiate between the terminology, Covariance
 30 or Coherency matrix, because the analysis presented is not affected by the selection of the
 31 basis.

32 In Pol-InSAR, the Pol-SAR covariance matrices are acquired separated by a spatial base-
 33 line. The two Pol-SAR covariance matrices can be defined as $T_{11} = \langle \underline{k}_1 \underline{k}_1^{*T} \rangle$ and $T_{22} =$
 34 $\langle \underline{k}_2 \underline{k}_2^{*T} \rangle$ and the Pol-InSAR covariance matrix (containing the interferometric information)
 35 is $T_{12} = \langle \underline{k}_1 \underline{k}_2^{*T} \rangle$ [5], [6].

36 An important operator in Pol-InSAR is the Pol-InSAR coherence defined as [5], [6]:

$$\gamma = \frac{\underline{\omega}^{*T} T_{12} \underline{\omega}}{\sqrt{\underline{\omega}^{*T} T_{11} \underline{\omega} \cdot \underline{\omega}^{*T} T_{22} \underline{\omega}}}. \quad (1)$$

37 A partial target contains a large amount of information and a parametrization can be ben-

eficial. In this paper, a parametrization proposed by Cloude and Pottier [18] is exploited for generating random Pol-SAR samples with Monte Carlo simulations. Please note, any other complete parametrization could be employed. The idea behind the Cloude-Pottier algorithm is to diagonalize the covariance matrix. In case of quad-polarimetric data (i.e. full scattering matrix) the decomposition is: $[T] = \sum_{i=1}^3 \lambda_i [U_i]$, where λ_i are the eigenvalues and $[U_i] = \underline{u}_i \underline{u}_i^{*T}$ are the eigenvectors. Please note, in this work reciprocity and monostatic system are assumed. The eigenvalues can be used to estimate the entropy (denoted as H) that helps recognize if there is a dominant SM: $H = -\sum_{i=1}^3 P_i \log_3 P_i$, where P_i are the probabilities of each eigenvalue and they are defined as $P_i = \lambda_i / (\lambda_1 + \lambda_2 + \lambda_3)$. Each of the eigenvectors can be represented using polar coordinates which provide the parametrization [12]: $\underline{u} = [\cos(\alpha), \sin(\alpha)\cos(2\beta)e^{j\mu}, \sin(\alpha)\sin(2\beta)e^{j\epsilon}]$. α is called the characteristic angle and β is the orientation angle. μ and ϵ are two phase angles with no specific physical interpretation.

II. QUADRATIC FORMS FOR POL-INSAR DATA

Given a generic $N \times N$ matrix A and a vector \underline{v} defined in an N dimensional space (e.g. \mathbb{C}^N), a quadratic form can be defined as $\underline{v}^{*T} A \underline{v}$ [19], [20]. It presents the combination of the second order elements of \underline{v} after transformation by the matrix A . Using quadratic forms, it is possible to study the sign of the matrix A . In the case of Pol-SAR, the covariance matrices are Positive Semi Definite. This means that their quadratic forms cannot be negative: $T \succeq 0$.

A. Integral of single quadratic form: Power

A generic partial target is a linear superposition of several scattering mechanisms (SM). In the case of monostatic quad-polarimetric acquisitions with reciprocal medium, the SM live

60 in a 3 dimensional complex space (\mathbb{C}^3) [3]. The latter constrains the covariance matrix to
 61 be 3×3 . Given a partial target, the power backscattered by a specific SM can be calculated
 62 considering the quadratic form of the covariance matrix T with an appropriate projection
 63 vector $\underline{\omega}$ that represents the SM:

$$P_{\underline{\omega}} = \underline{\omega}^{*T} T \underline{\omega} = \underline{\omega}^{*T} \underline{k} \cdot \underline{k}^{*T} \underline{\omega} \quad (2)$$

64 Such reasoning is central in the Cloude-Pottier decomposition where the SM with the
 65 maximum and minimum power are computed performing a diagonalization of the covariance
 66 matrix [3] (a proof can be easily obtained considering a Lagrangian optimization of the
 67 quadratic form). However, in some applications, we are not interested in the dominant SM,
 68 but in the average backscattering. The latter can be calculated solving the integral of the
 69 quadratic form varying the projection vector:

$$\frac{1}{S} \int_{\Theta} P_{\underline{\omega}} d\underline{\omega} = \frac{1}{S} \int_{\Theta} \underline{\omega}^{*T} T \underline{\omega} d\underline{\omega}, \quad S = \int_{\Theta} d\underline{\omega} \quad (3)$$

70 where Θ represents the support of the projection vector which is a unitary complex sphere.
 71 S is equal to the surface of such sphere and the integral is divided by S because we are not
 72 interested in the size of the support. In other words, we want that a unitary function (i.e.
 73 T equals to the identity matrix) provides a unitary integral. S can assume different values
 74 depending on the dimension of the space in which $\underline{\omega}$ lives (i.e. dual- or quad-pol data).
 75 Interestingly, it is not necessary to know the exact value of S for the following derivation.

76 The final solution of the integral is:

$$\frac{1}{S} \int_{\Theta} \underline{\omega}^{*T} T \underline{\omega} d\underline{\omega} = \frac{\text{Trace}(T)}{3} \quad (4)$$

77 where the operator $Trace[]$ represents the sum of the diagonal elements of a matrix. The
 78 derivation of the analytic solution is provide in the Appendix.

79 *B. Trace Coherence and the integral of Pol-InSAR coherence*

80 The Pol-InSAR coherence can be written using quadratic forms. This formalism allows
 81 to evaluate the Coherence Region (or Coherence loci), CoRe, which is a locus of points on
 82 the polar plot representing Pol-InSAR coherences (varying the projection vector) [3], [21].
 83 CoRe finds applications in modeling (e.g. Random Volume over Ground model [6]) and
 84 change detection [22]. A common way to estimate the CoRe is by performing a Monte
 85 Carlo simulation where a large number of random projection vectors $\underline{\omega}$ are generated. In
 86 the literature, methodologies were proposed to evaluate the extremes of the CoRe and the
 87 optimum polarizations [3], [23].

88 The center of mass of the CoRe (i.e. the average of all the coherence points) depends on
 89 the density of points inside the loci. This is defined as the integral:

$$\frac{1}{S} \int_{\Theta} \frac{\underline{\omega}^{*T} T_{12} \underline{\omega}}{\sqrt{\underline{\omega}^{*T} T_{11} \underline{\omega} \cdot \underline{\omega}^{*T} T_{22} \underline{\omega}}} d\underline{\omega}. \quad (5)$$

90 In this paper, a new operator named Trace Coherence is introduced:

$$\gamma_{tr} = \frac{Trace(T_{12})}{\sqrt{Trace(T_{11})Trace(T_{22})}} \quad (6)$$

91 Motivated by the previous result, we hypothesize that γ_{tr} can approximate the γ integral:

$$\frac{1}{S} \int_{\Theta} \frac{\underline{\omega}^{*T} T_{12} \underline{\omega}}{\sqrt{\underline{\omega}^{*T} T_{11} \underline{\omega} \cdot \underline{\omega}^{*T} T_{22} \underline{\omega}}} d\underline{\omega} \stackrel{?}{=} \gamma_{tr}. \quad (7)$$

92 It is clear, that the result obtained with a single quadratic form cannot be extended straight-
 93 forwardly, since the coherence operator is nonlinear. On the other hand, it is possible to
 94 prove that the previous equality holds when the matrices have some specific structures.

To investigate this, the eigenvector basis of the first covariance matrix T_{11} can be used to represent the space. Following the previous nomenclature, the integral can be rewritten as:

$$\frac{1}{S} \int_{\theta} \frac{\text{Trace} \left(T_{12} [AU_1 + BU_2 + CU_3 + \sum_{\substack{i,j=1 \\ i \neq j}}^3 \sigma_{ij} U_{ij}] \right)}{\sqrt{\text{Trace}(T_{11} [AU_1 + BU_2 + CU_3]) \text{Trace} \left(T_{22} [AU_1 + BU_2 + CU_3 + \sum_{\substack{i,j=1 \\ i \neq j}}^3 \sigma_{ij} U_{ij}] \right)}} d\omega. \quad (8)$$

The U_{ij} matrices multiplying T_{11} are not written because the product is traceless.

Looking at Eq. 8, it is possible to tell that the equality holds in the following situations:

Proof 1: $\sigma_1 T_{11} = \sigma_2 T_{22} = \sigma_3 T_{12}$, $\forall \sigma_i$ real scalar.

If the three matrices are equal but differ only by a scaling factor, the eigenvectors of T_{11} are able to vanish the off diagonal terms of T_{22} and T_{12} as well. Additionally, the values of A, B and C will be the same $\forall \omega$ (but a scaling factor that multiply A, B and C). They will therefore simplify and leave the expression equal to γ_{tr} . In practical terms, this happens when we are in the conditions of polarimetric stationarity (or Equi-Scattering Mechanism, ESM) and the interferometric decorrelation is independent of the SM. The CoRe will have the shape of a circle on the polar plot, with the mean and the peak of the density in the middle.

Proof 2: $T_{11} = \sigma T_{22}$ rank one $\forall \sigma$ real scalar.

If this is the case, the quadratic forms of the covariance matrix T_{12} will be forced to live in the same 1-D line of T_{11} and T_{22} which means we will be in the same situation of *Proof 1*. This result is also intuitive, since for a rank 1 covariance matrix the polarimetric process is deterministic and the CoRe collapses in one single point on the polar plot. The location of the point is determined by the interferometric

decorrelation.

Proof 3: $\sigma_1 T_{11} = \sigma_2 T_{22} = \sigma_3 I$, $\forall \sigma_i$, where I is the identity matrix (i.e. unitary polarimetric entropy).

This condition forces T_{12} to be diagonal (i.e. the polarimetric channels are not correlated independently on the interferometric information). In this situation, the off diagonal terms of all the matrices T_{11} , T_{22} and T_{12} vanish independently on the basis used. Moreover, A, B and C will be always equal to $\frac{1}{3}$, since each element of any orthonormal set will contain one third of the total matrix energy. Therefore, A, B, and C simplify and they leave the integral equal to γ_{tr} .

In all the other situations, it is not possible to prove mathematically that the integral is equal to γ_{tr} and therefore it has to be considered an approximation. Interestingly, *Proof 2* and *Proof 3* coincide with the boundary conditions for the polarimetric behavior of partial targets (completely polarized and de-polarized, respectively). Therefore, we may hope that intermediate situations will have similar behavior. In order to test the approximation, simulated and real data are exploited in the following.

C. Application of Trace Coherence

Before proceeding with tests, it is valuable to spend few words explaining some advantages of using γ_{tr} . From a general point of view, the main advantage of using γ_{Tr} compared to a single scattering mechanism solution (i.e. single channel, optimum polarization, extremes of CoRe) is that γ_{Tr} represents a synthetic information about the CoRe intrinsically based on the idea that the observed target is partial and therefore composed by several SM. With synthetic information it is meant a quantity that is able to combine, compact and synthesize a larger amount of information, which would otherwise need many more numbers.

137 This is done by integrating over all the possible realizations of the CoRe.

138 Therefore, γ_{Tr} may possibly find use in several applications where we need a single com-
139 plex number that can characterize in average the entire partial target without being linked to
140 one specific SM (e.g. the one with maximum coherence). Clearly, there are situations where
141 we are interested in identifying one specific SM and we do not want an averaged solution.
142 However, the possibility of having a rigorous way to evaluate the average coherence of an
143 entire partial target may be beneficial in some applications. In the following, few exam-
144 ples of some of these applications are mentioned. In terms of methodologies, γ_{Tr} could be
145 employed in change detection, classification and modeling.

146 (1) Coherent Change Detection (CCD) is a widely exploited methodology used to detect
147 small changes in targets that would not be detectable using Non-Coherent Change Detec-
148 tion (NCCD) [24]. With respect to CCD, some disadvantages may arise when a generic
149 polarization channel or the optimized polarization coherences are used. For instance, an
150 SM may have a very small coherence because the observed target is orthogonal to the
151 selected SM (i.e. we are observing noise). In this case a detection will be triggered even
152 though the actual target is stationary. The center of mass however takes into account all
153 the components of the partial target weighted by their intensity, providing therefore a
154 synthetic information of the target as a whole.

155 (2) Still in the context of change detection, the CoRe keeps valuable information regarding
156 the phase center as well. Recently, it has been shown that the difference between DEM
157 obtained by single pass TanDEM-X data can be used to extract information regarding
158 large vertical movements of the observed target. This methodology is often referred
159 to as Differential DEM [25]. For instance, differences between DEM can be used to
160 monitor water level changes in wetlands. Different polarization channels may provide

dissimilar estimates of this movement. This is because, different SM in the partial target can have generally distinct projections on the single channels that are used for the estimation. Predicting the amount of such projections can be rather hard and generally requires powerful physical models. On the other hand, the phase of γ_{Tr} represents the entire average of phase centers that can be attributed to the entire partial target. In absence of appropriate models, the phase of γ_{Tr} may provide more robust results because it is supposed to average out (with proper weights) the results that each single channel may give.

(3) In the context of classification, the multi-baseline investigation of volume structure is a topic of interest [26], [27]. A possible use of γ_{Tr} could be to extract "structure indexes" based on the combination of selected points inside the CoRe. For instance, the distances of γ_{Tr} to the lines that cross the CoRe extremes or optimum polarizations, could bring information regarding the distribution of points inside the CoRe without calculating the histogram of the CoRe elements (which is time consuming).

(4) As mentioned previously, CoRe are used in modeling. In the Pol-InSAR retrieval of vegetation height, we are often interested in identifying the line that crosses the CoRe and represents the Random Volume over Ground (RVoG) model [6], [28], [29]. For instance, knowing the CoRe center could help retrieving some extra information to obtain the line. Or it could help understanding when RVoG model is not applicable.

(5) The integral is obtained summing elements and therefore it is expected to have less speckle. Theoretically, compared to a generic polarization channel the Equivalent Number of Look (ENL) can be increased by a factor up to 3: $ENL_{sing} \leq ENL_{tr} \leq 3ENL_{sing}$, where ENL_{sing} and ENL_{tr} are respectively the ENL for a single channel and γ_{tr} . The left equality holds when the rank is 1. In other words, the sum of the

three components does not increase the ENL when the three components are linearly dependent, which is the definition of a rank one matrix. The right equality holds when the process is completely depolarized (i.e. *Proof 2*). This is because the three components are independent each other. Among other situations, increasing ENL is valuable for change detection, where the attention is focused on low values of coherence that are biased when the ENL is low [30].

(6) Another way to determine the CoRe center is by using a Monte Carlo Integration, MCI (i.e. the CoRe is generated with a Monte Carlo simulation and all the points are averaged together). Compared to the MCI, γ_{tr} is much faster, since it only requires a very limited amount of multiplications (it does not require the construction of the CoRe).

III. SENSITIVITY ANALYSIS WITH SIMULATED DATA

In this section, a sensitivity analysis is performed by means of a Monte Carlo method. Some preliminary results on such analysis can also be found in [31].

A. Monte Carlo Simulations

The simulations performed in this work assume the scattering vectors to be Gaussian. The impact of different types of texture could be investigated in the future.

The simulations were performed as follows:

(1) A Monte Carlo method is used to generate N realizations of scattering vectors drawn by a 3D-Complex Gaussian distribution. This is performed twice (one for each acquisition).

Therefore, we generate two sets of "white random vectors": $\underline{k}_1^w(i)$ and $\hat{\underline{k}}_2^w(i)$, where $i = 1, \dots, N$.

(2) For each component of the vectors $\underline{k}_1^w(i)$ and $\hat{\underline{k}}_2^w(i)$ the interferometric correlation and phase difference is selected. This allows to model the shape of the coherence loci on the

- 208 polar plot. The way this is done is by generating $\underline{k}_2^w(i) = \underline{a} \circ \underline{b} \circ \underline{k}_1^w(i) + (\underline{a} - \underline{1}) \circ \hat{\underline{k}}_2^w(i)$,
 209 where \underline{a} is a 3 dimensional real vector with each element included in the interval $[0, 1]$,
 210 \underline{b} is a 3 dimensional complex vector with elements $[e^{-j\phi_1}, e^{-j\phi_2}, e^{-j\phi_3}]$, $\underline{1} = [1, 1, 1]^T$
 211 and \circ is the Hadamard (or element-wise) product. \underline{a} and \underline{b} contain information regarding
 212 respectively interferometric correlation and phase differences of the three simulated SM.
- 213 (3) The white random vectors are colored using two asymptotic covariance matrices \dot{T}_{11} and
 214 \dot{T}_{22} (representing the partial targets observed in the two acquisitions): $\dot{T}_{11}^{\frac{1}{2}} \underline{k}_1^w(i) = \underline{k}_1(i)$
 215 and $\dot{T}_{22}^{\frac{1}{2}} \underline{k}_2^w(i) = \underline{k}_2(i)$
- 216 (4) The simulated Pol-InSAR matrices are calculated by averaging N realizations of the
 217 outer product of the simulated vectors: $T_{11} = \langle \underline{k}_1 \underline{k}_1^{*T} \rangle_N$, $T_{22} = \langle \underline{k}_2 \underline{k}_2^{*T} \rangle_N$ and $T_{12} =$
 218 $\langle \underline{k}_1 \underline{k}_2^{*T} \rangle_N$, where $\langle \cdot \rangle_N$ is the finite average of N realizations. Since the simulation pro-
 219 vides random variables that are close to be independent, the value of ENL can be ap-
 220 proximated by N. In the real scenario, the realizations would be neighbor pixels and the
 221 average would be done by a spatial filter (e.g. a boxcar).
- 222 (5) Points 1 to 4 are repeated K times to evaluate statistics. They represent K experiments.
 223 In other words, a set of K covariance matrices is produced: $T_{11}(k)$, $T_{22}(k)$ and $T_{12}(k)$,
 224 with $k = 1, \dots, K$. Each of these realizations is slightly different due to speckle.
- 225 (6) For each of the K experiments, the CoRe is evaluated considering L random vectors from
 226 the support of $\underline{\omega}$ (sampled uniformly using a Monte Carlo sampling). This means that for
 227 each triplet $T_{11}(k)$, $T_{22}(k)$ and $T_{12}(k)$ we will have one CoRe and each experiment will
 228 have a slightly different CoRe due to speckle. Beside visualization purposes, L decides
 229 the amount of points used to evaluate the Monte Carlo Integral (MCI).
- 230 To summarize, K experiments are performed averaging N realizations and for each exper-

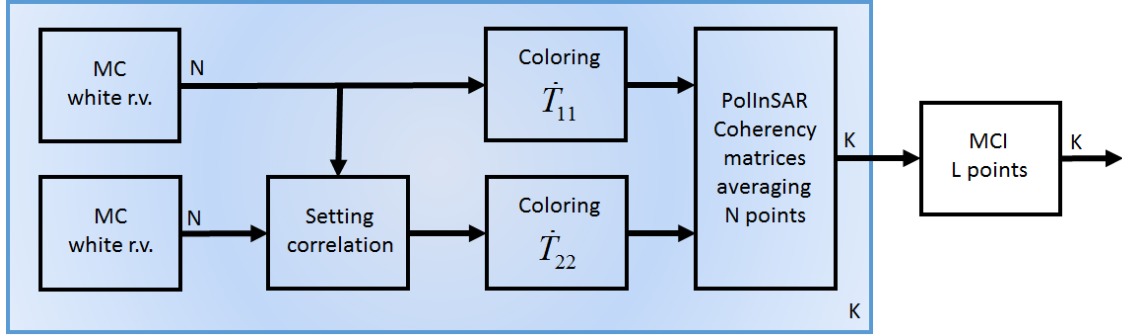


Fig. 1. Block diagram for the Monte Carlo simulations. MC: Monte Carlo; r.v.: random variables; MCI: Monte Carlo Integral. N, K (on top of the arrows) indicate the number of elements flowing out the block.

231 iment the CoRe is evaluate using L points. A block diagram of the simulation procedure is
 232 presented in Figure 1.

233 For the sake of simplicity, we concentrate on simulations with the assumption of ESM:
 234 $\dot{T}_{11} = \dot{T}_{22}$. Please note, even though the matrices T_{11} and T_{22} are very similar, they will never
 235 be exactly the same due to speckle. There are several reasons why we decided to concentrate
 236 on ESM simulations. Firstly, the ESM case is generally of most interest for modeling, since
 237 changes in the polarimetric behavior would naturally lead to low values of coherence that
 238 cannot be used for retrieval. Secondly, considering $\dot{T}_{11} \neq \dot{T}_{22}$ would increase substantially
 239 the amount of tests we will need to carry out in order to be complete and this cannot be
 240 contained in one single paper. Thirdly, it would be very hard to provide satisfactory physical
 241 interpretations of non-ESM tests, because the understanding of how different partial targets
 242 combine to build up the T_{12} matrix is still not well understood. However, to have some
 243 feeling regarding the approximation behavior for no-ESM targets, a few tests are shown in
 244 the following.

245 In the following tests, $K = L = 500$ and $N = 60$ (unless differently stated). The
 246 parameters K and L are selected taking into account accuracy and execution time. In the
 247 tests performed, $K = 500$ representations revealed to be sufficient to extract the underlying

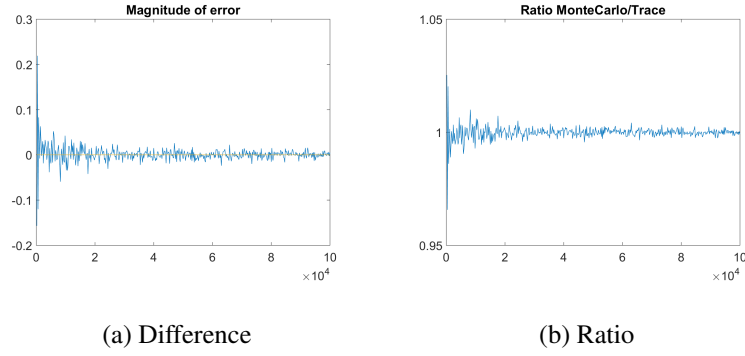


Fig. 2. Simulated dataset. Integral of power. (a) $MCI - Trace/3$; (b) $\frac{MCI}{Trace/3}$

248 statistics of the covariance matrices. On the other hand, $L = 500$ points for the Monte Carlo
 249 integration provides a negligible error in estimating the integral. Finally, L was selected
 250 equal to 60 to approximately match the ENL of the test with real data.

251 A.1 Integral of Power

252 The first test is aimed at evaluating the correctness of the integral derivation for a single
 253 quadratic form. $K = 500$ realizations of a covariance matrix T are generated and for each
 254 one the MCI is performed using L realizations of the quadratic form. Interestingly, the
 255 difference between the MCI and the third part of the trace depends on L , the number of
 256 points used to estimate the integral. The difference reduces to numbers closer to the machine
 257 error when L increases. Only when L is large enough the support of the integral is covered
 258 properly. The results for a generic covariance matrix are shown in Figure 2. If $L = 10^6$, then
 259 the difference reduces to $7.1 \cdot 10^{-5}$ and the ratio to 1.0000. As a final remark, this experiment
 260 should clarify that the MCI is a very good approximation of the integrals (we believe better
 261 than γ_{tr} as shown in next section), but it is not immune from errors. Therefore, part of the
 262 errors that we estimate in next sections could be related to the MCI.

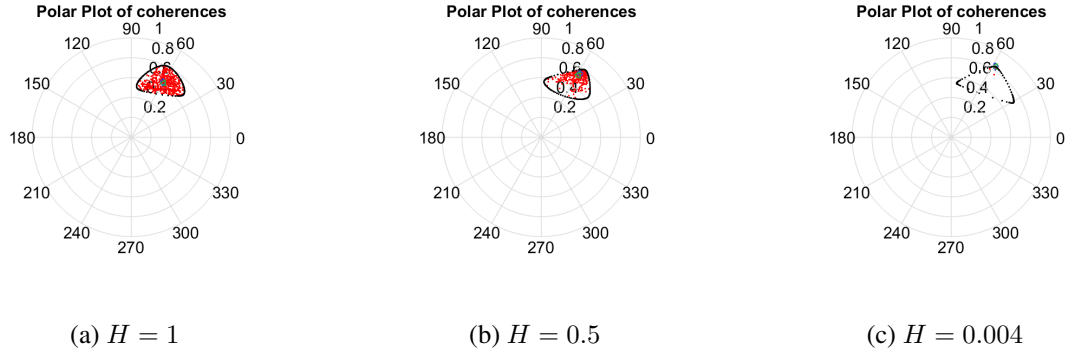


Fig. 3. Simulated dataset. Coherence Regions varying the entropy: (a) $H = 1$; (b) $H = 0.5$; (c) $H = 0.004$

A.2 Entropy

It was shown that the equality between γ_{tr} and the integral of γ holds when the entropy of both covariance matrices is either 0 or 1. In this section we would like to put this under test.

The simulator was used to generate CoRe with triangular shapes. This is for the sake of generality, but the results are similar when ellipses are used. Figure 3 shows three CoRe when the entropy is respectively $H = 1$, $H = 0.5$ and $H = 0.004$. In this simulations, the dominant target is always a surface (i.e. $\alpha = \beta = 0$). The next section provides more details regarding the selection of the second and third scattering mechanisms. The change in entropy is obtained fixing the second and third eigenvalues to be equal and increasing the first eigenvalue.

In Figure 3, the red points represent the elements of the CoRe, while the black points are the CoRe boundary. The blue diamond is the trace coherence γ_{tr} and the green triangle is the Monte Carlo Integral (MCI). The shape of the CoRe is triangular (as expected) and the location is about the same in each experiment. Please note, the CoRe moves in different experiments due to speckle. It can be noticed that the density of points inside the physically feasible region (the boundary of the CoRe) changes substantially when the entropy is modified. Specifically, an entropy equal to one returns a more homogeneous distribution of points,

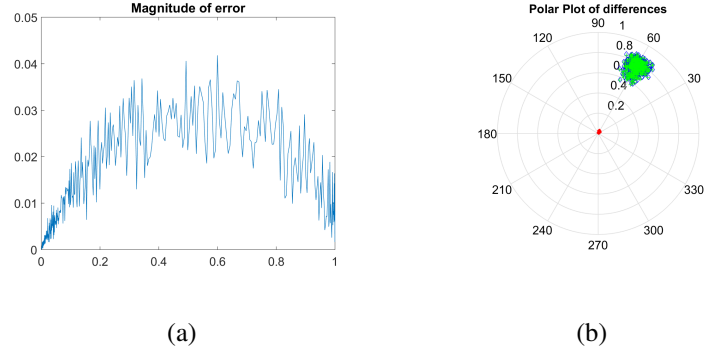


Fig. 4. Simulated dataset. (a) Difference between γ_{tr} and MCI; (b) Difference represented on polar plot, Blue: $\gamma_{tr}(k)$, Green: $MCI(k)$ and Red: errors

while an entropy close to zero returns a process that is polarimetrically more deterministic and therefore it does not exhibit significant variation (almost one single point on the polar plot).

From Figure 3, it is possible to observe that γ_{tr} is well aligned to MCI for very high or low entropy values. To have a more quantitative analysis, in Figure 4.a the difference is plotted as a function of the entropy. This is calculated as $\Delta = |\gamma_{tr}(k) - MCI(k)|$, where k is the index representing the realization. Δ is generally smaller than 0.03 and reduces when it approaches $H = 1$ and $H = 0$. This means that γ_{tr} is an excellent approximation for $H = 0$ and $H = 1$, while it performs worse at intermediate values of H . To have a comparison between the approximation error and the actual estimated values, Figure 4.b displays $\gamma_{tr}(k)$ and $MCI(k)$ for all the K experiments. $\gamma_{tr}(k)$ are in blue, $MCI(k)$ are in green and the errors are the red points (at the center of the polar plot). The green diamonds are always plotted on the foreground of the blue ones. Therefore, if the two points overlap, the blue diamond may be less visible. It can be observed that the errors are more than one order of magnitude smaller than the actual coherence values.

A.3 Scattering Mechanisms

In this section, we concentrate the tests on $H = 0.5$, since this seems to be the worst scenario in terms of entropy.

We want to analyze the effect of using different SM to simulate the partial target. The entropy is kept equal to 0.5 and the dominant SM \underline{u}_1 is rotated. The second and third SM \underline{u}_2 and \underline{u}_3 are kept orthogonal to the first one using a Gram-Schmidt ortho-normalization [20]. Additionally, we fixed $\lambda_2 = \lambda_3$ to make sure that vectors on the plain orthogonal to \underline{u}_1 do not have preferential directions, that could produce less general results. Finally, the interferometric phase and decorrelation of each of the three \underline{u}_i is kept the same, despite the fact that the \underline{u}_i represents a different target.

Following the Cloude-Pottier decomposition, different values of α_1 and β_1 are tested. For the sake of brevity only the analysis of α_1 is presented.

Figure 5.a presents the CoRe for $\alpha = 0$, $\alpha = 45$ and $\alpha = 90$. Interestingly, the three CoRe appears to be rather similar, with a triangular shape and points concentrated in the upper right corner. The variation between the different CoRe is only due to speckle, because they use the same underlying covariance matrix to generate the Monte Carlo realizations. Figure 6.a presents the error Δ as defined previously. Interestingly, this is always around 0.03. The fluctuation can be explained because each experiment has slightly different covariance matrices (due to speckle) that therefore generate slightly different CoRe. It can be inferred that the error is independent of the specific SM. Abstracting this result, we could say that the center of mass of the CoRe is invariant to change of basis, which is a well-known property for the Pol-InSAR coherence (i.e. the γ of a selected SM is basis invariant). Such property can also be easily proofed using the definition of γ_{tr} and noticing that the Trace is basis

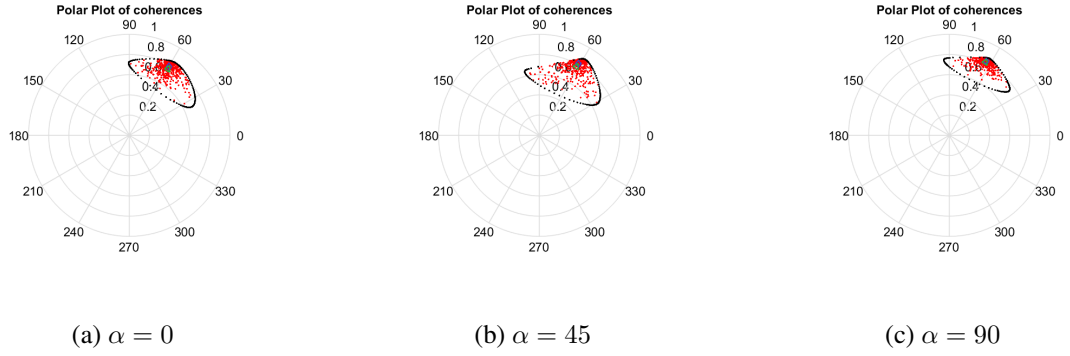


Fig. 5. Simulated dataset. Coherence Regions varying α : (a) $\alpha = 0$ (b) $\alpha = 45$ (c) $\alpha = 90$

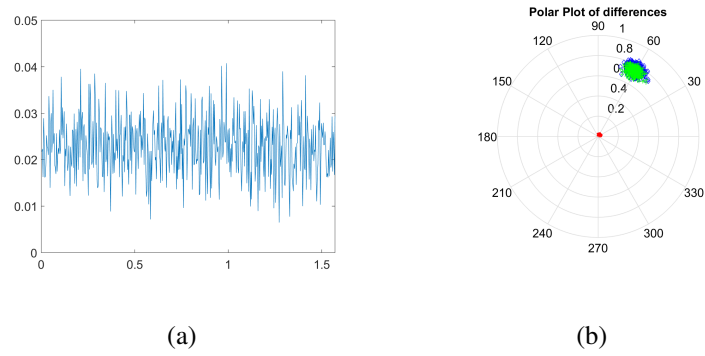


Fig. 6. Simulated dataset. Error changing the scattering vector. (a) Difference between γ_{tr} and MCI; (b) Difference represented on polar plot, Blue: $\gamma_{tr}(k)$, Green: $MCI(k)$ and Red: errors

invariant.

Figure 6.b presents a comparison of the error with the actual estimated value.

A.4 Interferometric decorrelation

This section investigates the dependency of the approximation to the shape of the CoRe. In particular, the CoRe is stretched along the radial direction of the polar plot changing the interferometric decorrelation of one SM. The entropy is fixed to 0.5 and an ESM hypothesis is made. Please note, the word "decorrelation" is here used to identify the magnitude of the interferometric coherence.

The three SM are built as follow. The dominant SM is fixed and it has an eigenvalue 10 times stronger than the others, which provides an entropy of approximately 0.5. Its interfer-

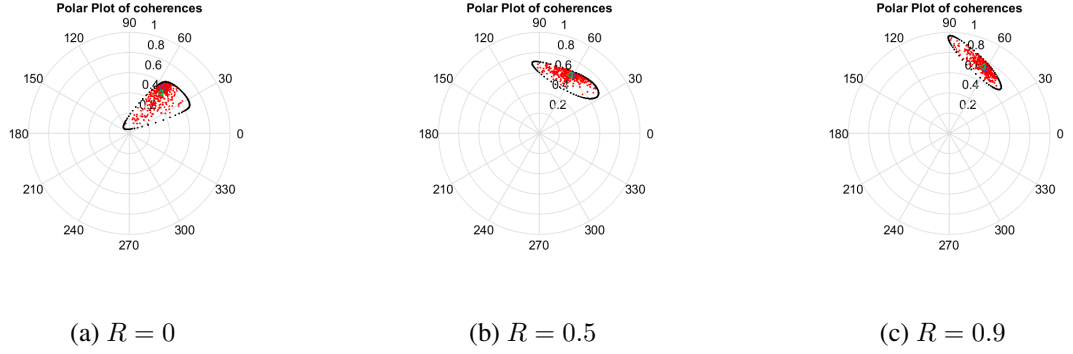


Fig. 7. Simulated dataset. Coherence loci varying the decorrelation of one scattering mechanism: (a) $R = 0$;

(b) $R = 0.5$; (c) $R = 0.9$

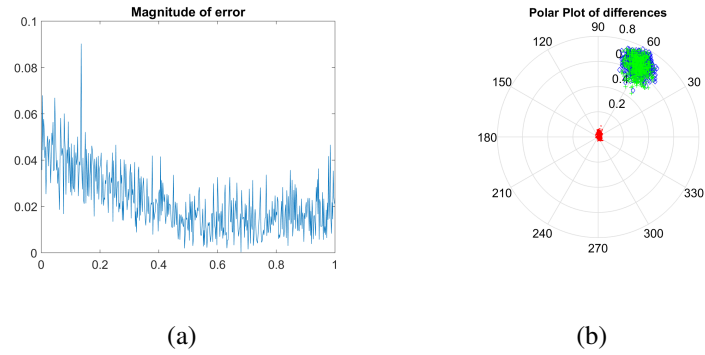


Fig. 8. Simulated dataset. Changing decorrelation. (a) Difference between γ_{tr} and MCI; (b) Difference represented on polar plot, Blue: $\gamma_{tr}(k)$, Green: $MCI(k)$ and Red: errors

ometric coherence is set to a phase of 60 degrees and decorrelation of 0.5. The second SM is fixed and it has a interferometric phase of 30 degrees and decorrelation of 0.5. The third SM is modified. Its interferometric phase is 90 degrees, but the decorrelation varies from 0 to 1. In order to observe how the CoRe varies, Figure 7 presents the polar plot for values of decorrelation R equal to 0, 0.5 and 0.9. It is possible to observe that the left tip of the region moves from 0 to 0.9.

The magnitude of the error is presented in Figure 8.

It is possible to observe that the error depends on R . In particular, it is minimum around $R = 0.5$, that is, when the moving SM is more aligned with the other two. The error increases when the loci are more stretched and the point density is less uniform. Fortunately, even in

the worst conditions, the error seems to be in mean around 0.04.

A.5 Worst case scenario

We want to devise an experiment that is the most challenging for the approximation. Please note, the simulations performed in this section are likely to be unrealistic and they only purpose is to gain understanding of the approximation. Therefore, we are not suggesting that the peculiar shapes presented in this section could be observed in real data.

We want to create a point density that is largely unbalanced inside the CoRe. A way to achieve this is by using very low values of entropy. However, it was observed that the CoRe collapses to a single point when $H = 0$. Therefore, the entropy is selected as $H = 0.1$. In terms of eigenvalues, the dominant SM contains 100 times more power than each of the other two SM. The second and third eigenvectors have an interferometric phase of 90 and 180 degrees (respectively) and a decorrelation of 0.9. A value of 0.9 is unrealistic, since their eigenvalues are very low (they should be affected by noise) and their phases are very different (which would suggest large volume or multiple scattering decorrelation). The dominant SM is set to have a decorrelation of 0.9 and an interferometric phase that varies from 0 to 360 degrees.

Figure 9 shows how the CoRe reshapes when the interferometric phase is varied. The most of the points are concentrated in the location of the dominant SM, nevertheless the CoRe is designed to stretch till the other two SM.

Figure 10 shows the error, which depends on the angle. The lowest error is approximately 150 degrees, while largest errors are for values of 0 or around 300 degrees. The largest errors correspond to the most stretched CoRe. This can also be noted plotting the differences on a polar plot. It is encouraging to observe that even in such unrealistic experiment the errors

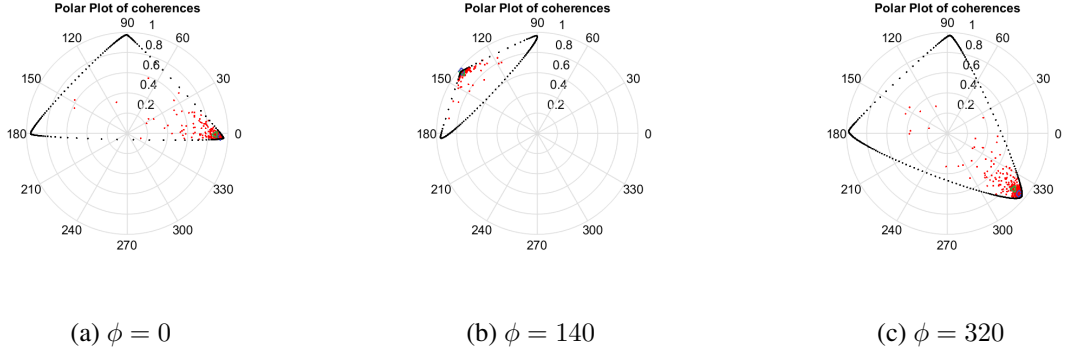


Fig. 9. Simulated dataset. Coherence loci varying the interferometric phase of the dominant scattering mechanism: (a) $\phi = 0$; (b) $\phi = 140$; (c) $\phi = 320$ (degrees).

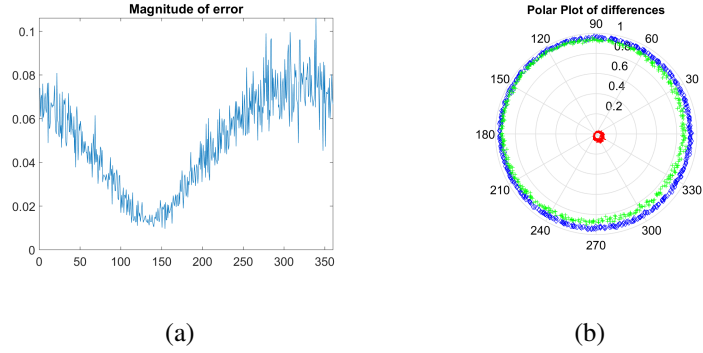


Fig. 10. Simulated dataset. Changing interferometric phase. (a) Difference between γ_{tr} and MCI; (b) Difference represented on polar plot, Blue: $\gamma_{tr}(k)$, Green: $MCI(k)$ and Red: errors

appear to be contained in values lower than 0.09.

A.6 Peak of the histogram

Figure 10.b offers another engaging insight that was not discussed in the previous section. From Figure 10.b is possible to observe that $\gamma_{tr}(k)$ are always larger (in magnitude) than $MCI(k)$. In the latter experiment, the point distributions have large skewness with shorter tails that are always closer to the unit circle. This lead to the idea of testing the relationship between $\gamma_{tr}(k)$ and the peak (i.e. or mode) of the CoRe $Peak(k)$. Please note, the word "mode" may be an abuse of notation because it requires interpreting the CoRe as a random process. This is true when the loci are obtained by a Monte Carlo method, but in general it

is more proper to talk about point density as deterministic 3-D surfaces on the polar plot.

In order to test this idea, the point density is estimated with a histogram and the peak location is determined. Care was taken to have the histogram bin size small enough to accurately capture the peak location, but not too small to produce a jagged histogram. Once the peak location is determined, the differences between $Peak(k)$ and $\gamma_{tr}(k)$ or $MCI(k)$ are evaluated as: $\Delta_{tr} = |\gamma_{tr}(k) - Peak(k)|$ and $\Delta_{MCI} = |MCI(k) - Peak(k)|$. Figure 11 shows the results of such analysis where the red points represent Δ_{tr} and the blue points are Δ_{MCI} .

$\gamma_{tr}(k)$ seem to be consistently closer to the peak compared to $MCI(k)$. Remarkably, Δ_{tr} remains very small even in this worst case scenario. The difference Δ_{tr} , Δ_{MCI} are also estimated using the simulations of the other experiments (i.e. varying entropy and decorrelation). Again, $\gamma_{tr}(k)$ are consistently closer to the peak than $MCI(k)$. Observing the latter results it is evident that the estimation of the peak can be very challenging and unreliable. When the entropy grows, the density of points become rather uniform in the CoRe. The density surface still has a peak determined by the location of the dominant SM, or the middle point of equal SM, but the surface gradient can be rather low. This means that estimating the peak using histograms becomes unreliable. This is the reason why the difference between γ_{tr} and $MCI(k)$ can be smaller than the difference between γ_{tr} and the peak when the entropy grows (i.e. the location of the peak is not well estimated). The situation improves (i.e. Δ_{tr} reduce to a maximum of 0.02) when L, the number of points used in the CoRe, becomes very large (e.g. 10000), but the computational time also increases from less than a minute to tens of minutes (using Matlab on a computer with 16 GB of RAM and 3.6 GHz of clock).

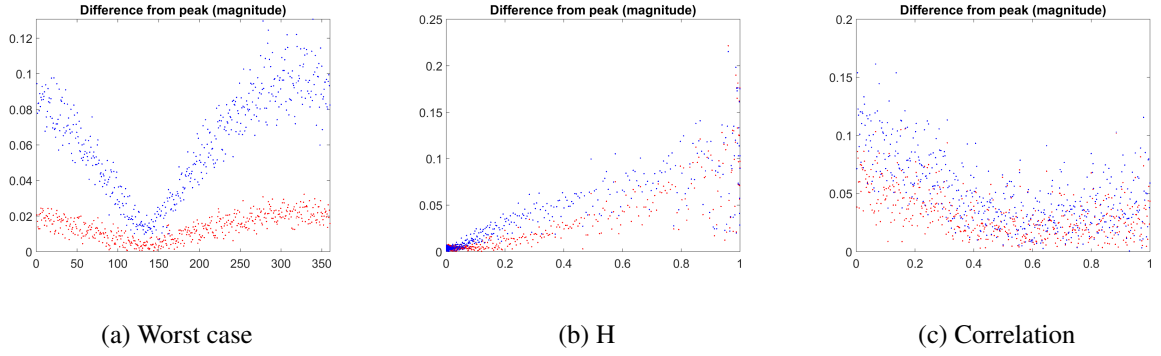


Fig. 11. Simulated dataset. Red: difference between Peak and γ_{tr} , Blue: difference between Peak and MCI.

(a) Worst scenario; (b) Varying entropy (as previous experiment); (c) Varying decorrelation (as previous experiment)

A.7 Changing the ENL

The final test is focused on the ENL. In the previous experiments the value $N = 60$ was used, since this should capture a real scenario where a boxcar of around 9×9 is used (please note, pixels of a SAR image are not independent). However, it is interesting to test the dependency of the approximation with respect to N .

A partial target with $H = 0.5$ and a triangular CoRe (same as the one used in the test of entropy) is simulated. The value of N is varied between 3 and 500. Figure 12 presents the magnitude of the difference Δ . Interestingly, it appears that the approximation is in average rather independent of the ENL for values higher than 10. For ENL below 10 the approximation seems to have lower performance. This is because very low values of ENL can enlarge significantly the CoRe and the approximation is affected by the size of the CoRe. However, above a sorter ENL value (in this case around 10) the mean error remains rather constant. On the other hand, the error variability is dependent on the ENL, but seems to become rather constant after around 200 ENL. We do not expect the error to go to zero for very large ENL because the CoRe does not collapse to a single point (i.e. the shape is determined by the SM locations).

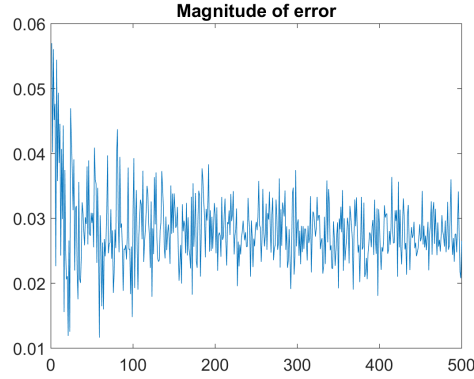


Fig. 12. Simulated dataset. Estimation error varying the ENL between 3 and 500

As a final remark, in practical scenarios, we may expect that the approximation can show larger dependency on the size of the boxcar window. Larger windows are more likely to include different targets that impacts the entropy and a change in entropy affects the approximation as showed in previous sections.

A.8 Polarimetric non-stationarity

Previous sections adopted the ESM assumption. In this section, we want to gain some understanding regarding the approximation when the ESM hypothesis is not fulfilled. Figure 13 displays the results of two tests.

- (1) The SM of the partial targets stay the same. The entropy of the first target is $H^I = 0.5$ and the entropy of the second target is varied between 0 and 1 ($H^{II} \in [0, 1]$).
- (2) The entropy of T_{11} and T_{22} is 0.5. The dominant α of the first target is $\alpha_1^I = 0$ and the dominant α of the second target is varied between 0 and 90 degrees ($\alpha_1^{II} \in [0, 90]$).

As expected, the approximation is dependent on the specific selection of the two partial targets. The error depends on the CoRe shape and density that change when the partial targets are modified. Unfortunately, it is rather hard to interpret these results except for few comments. Apparently, the error still reduces when the entropy of one of the two targets is

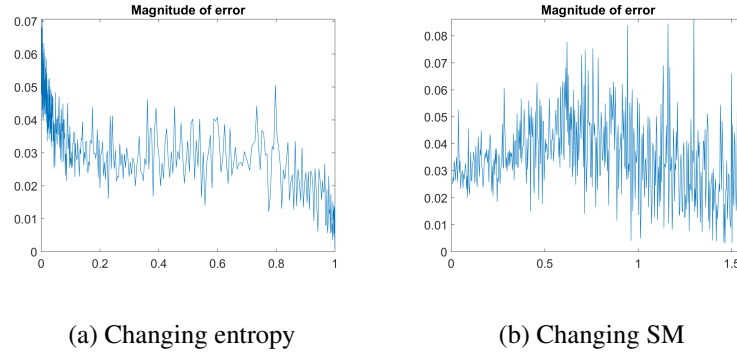


Fig. 13. Simulated dataset. Testing non-ESM. (a) Changing the entropy of the second target; (b) Changing the SM of the second target

unitary. If the two partial targets become more different the fluctuation of the error (due to speckle) is larger. This is because the structure of the T_{12} matrix becomes more variable.

As a final remark, it is important to keep in mind that the way non-ESM targets are simulated can impact strongly the analysis. In this work, we set that the projection of the second partial target over the first maintains the same correlation. This is to say that the second partial target is obtained by the first one plus an additive component (that is clearly uncorrelated with the first target). This therefore does not cover the case when the first target is substituted by a completely new second target. The latter scenario will show a much larger decorrelation and we may expect that the CoRe will cluster around the zero in a uniform way. This should improve the approximation.

A.9 Summary of simulations

It was observed that the approximation depends on the CoRe shape and point density.

Further experiments showed that γ_{tr} is significantly biased toward the peak of the density at a level that it could be possible that γ_{tr} represents the peak. Unfortunately, proving this property is not trivial, unless the peak and mean have the same location. This happens in the following situation:

440 (1) ESM hypothesis and single decorrelation mechanism: the CoRe is a circle with a sym-
 441 metric density

442 (2) The entropy is unitary: even if the distribution is rather smooth, the peak and the mean
 443 would both be the middle point between the three scattering mechanisms.

444 (3) The entropy is null: in this case, the CoRe collapses to a single point

445 The previous conditions are the same in which it was possible to proof that γ_{tr} is equal to
 446 the integral.

447 As a final remark, in some applications, knowing the location of the peak may be even
 448 more beneficial than the mean. For instance, if the long tail of the distribution represents SM
 449 that are not of interest (e.g. because they represent noise) we may like to have a result that is
 450 slightly closer to the dominant SM.

451 IV. TEST ON REAL DATA

452 A. *Presentation of Data*

453 The data exploited in this analysis were acquired by the E-SAR (DLR) system in L-band,
 454 during the AgriSAR 2006 campaign. The dataset is quad-polarimetric and presents several
 455 flight passes over agricultural areas near the village of Grömin in the North of Germany.
 456 Some preliminary test of γ_{tr} on the AGRISAR dataset can be found in [32].

457 The main parameters of the acquisitions exploited in this work are shown in Table I.

458 Figure 14 shows the RGB Pauli images of a portion of the entire scene that will be used
 459 as initial test area. The two acquisitions considered here were carried out the 13th of June
 460 and the 5th of July and they have a nominal baseline equal to zero. However, in the exploited
 461 data, there is still a residual baseline. In the future some test will also be focused on baselines
 462 largely different from zero. The scene presents several agricultural fields with some buildings

TABLE I

ESAR AGRISAR 2006 ACQUISITIONS EXPLOITED.

Acquisition time	Band	Slant range resolution	Azimuth resolution	Polarization
19/04/06	L	2 <i>m</i>	0.9 <i>m</i>	Quad-pol
13/06/06	L	2 <i>m</i>	0.9 <i>m</i>	Quad-pol
21/06/06	L	2 <i>m</i>	0.9 <i>m</i>	Quad-pol
05/07/06	L	2 <i>m</i>	0.9 <i>m</i>	Quad-pol

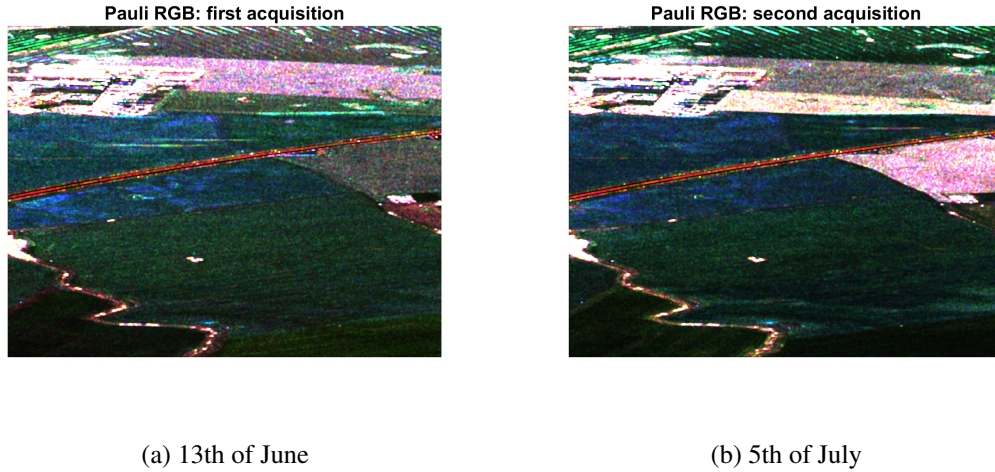


Fig. 14. AGRISAR dataset, L-band (E-SAR). Pauli RGB images: (a) 13th of June; (b) 5th of July. Boxcar filter: 9x9 pixels.

(farms). The color coding of the Pauli RGB is Red: $\frac{1}{\sqrt{2}}\langle|HH - VV|^2\rangle$, Green: $\sqrt{2}\langle|HV|^2\rangle$,
 Blue: $\frac{1}{\sqrt{2}}\langle|HH + VV|^2\rangle$.

It can be observed that some of the fields have experienced a change between the two acquisitions, while others appear to be rather stationary. Also, the image contains bright point targets that allow to test a variety of entropy values.

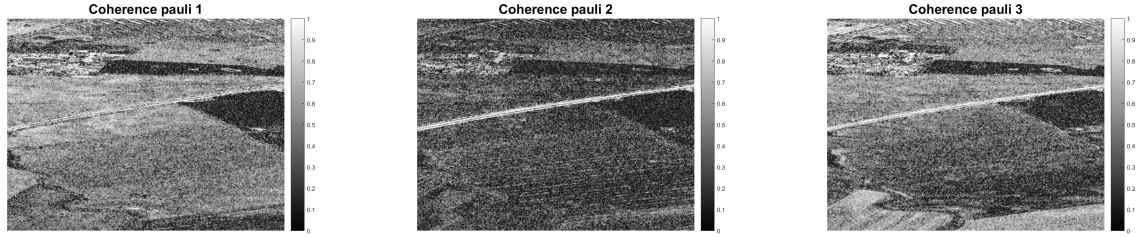
(a) $HH + VV$ (b) $HH - VV$ (c) HV

Fig. 15. AGRISAR dataset, L-band (E-SAR). Magnitude of interferometric coherences for the Pauli basis: (a) $HH + VV$; (b) $HH - VV$; (c) HV . Boxcar filter: 9×9 pixels.

B. Comparison of coherences

Before visualizing the Trace Coherence γ_{tr} , it is interesting to display coherences for standard targets. The interferometric coherences for the three elements of the Pauli basis are shown in Figure 15. For this a boxcar filter of 9×9 pixels is used. It is apparent that changing the projection vector the coherence can vary substantially. Specifically, the first component of the Pauli decomposition (that is referred as Odd-bounce or surface) is the most correlated, while the even-bounce (or horizontal dihedral) seems to be the weakest for most of the fields. Also, the cross-polarization channel (which is often associated with volume scattering) is stronger than the dihedral scattering (since there is a volume component), but it is lower than the surface scattering, since it suffers more from volume decorrelation. Additionally, all the SM which present a low backscattering (e.g. HV channel on bare ground) will suffer from noise decorrelation.

The images for the wrapped interferometric phases are reported in figure 16.

Figure 17 compares the results with γ_{tr} . The magnitude and phase of γ_{tr} are somehow in between the ones of the Pauli basis. It is possible to notice, that dark areas in all the channels appear darker in γ_{tr} . This is because we are able to increase the number of equivalent looks

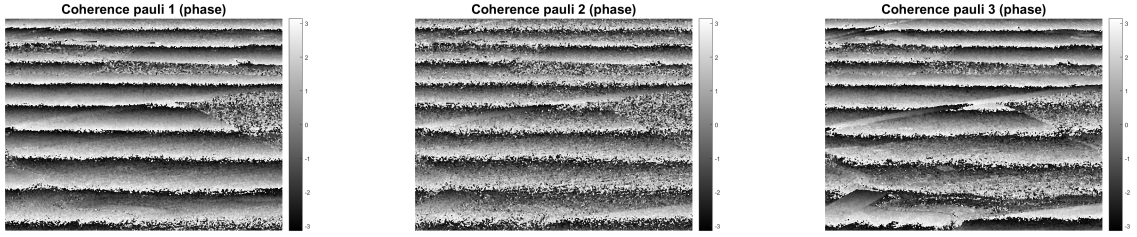
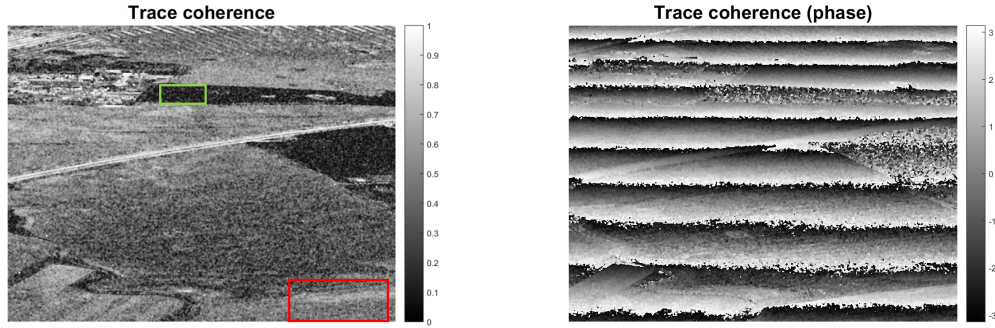
(a) $HH + VV$ (b) $HH - VV$ (c) HV

Fig. 16. AGRISAR dataset, L-band (E-SAR). Phase of interferometric coherences for the Pauli basis: (a) $HH + VV$; (b) $HH - VV$; (c) HV . Boxcar filter: 9x9 pixels.



(a) Module

(b) Phase

Fig. 17. AGRISAR dataset, L-band (E-SAR). Magnitude and phase of the trace coherences γ_{tr} . Boxcar filter: 9x9 pixels.

reducing the coherence bias for low values. An important point to observe is that γ_{tr} does not introduce any apparent bias or artifact in the image. This is because, γ_{tr} synthesizes the information contained in the different channels (i.e. evaluate the integral), but it does not introduce information that is not present in any of the polarimetric channels.

Comparing the magnitude of γ_{Tr} with the coherence magnitudes of the Pauli components, it is possible to observe one of the advantages of using γ_{Tr} . The red rectangle (bottom right corner) represents an area where we could expect volume scattering due to the green color in both RGB images. The combinations $HH+VV$ and $HH-VV$ have rather low backscat-

tering and therefore are strongly affected by noise. If a copolar channel would be used to detect changes, the algorithm would probably call a detection (clearly depending on how the threshold is set). However, since the dominant mechanism appears to be a SM that provides higher HV backscattering, the detector should rely more on the use of the cross-polar channel compared to the co-polar channels. γ_{Tr} allows to perform this weighting without the need of knowing the physical model that characterize the target under observation. This is because γ_{Tr} averages the coherence of each SM based on the weight that they have in terms of backscattering. The HV channel contains the most of the power of the partial target and therefore it has a higher weight in the integral. The physical reason behind this is that the distribution of points in the CoRe is ruled by the relative strength of the scattering mechanisms composing the partial target (i.e. points tend to concentrate around the dominant SM).

Finally, it is possible to observe how γ_{Tr} may improve the ENL (and therefore the estimation) in areas where all the channels are decorrelated. The green rectangle (upper part of the figure) identifies an area that is suffering change (this is clearly visible in the Pauli RGB images). The magnitude of the coherences in the Pauli bases has an average value of approximately 0.22, while the magnitude of γ_{Tr} for the same area is approximately 0.16.

C. Evaluation of error

This final section is dedicated to estimate the approximation error. Figure 18 shows the CoRe for three generic points in the image covering winter wheat and field grass. The latter are just a few representatives of the shapes that we can encounter in this dataset. Due to the fact that we are often in the condition of polarimetric non-stationarity (i.e. the ESM hypothesis is often not fulfilled), the loci can assume shapes that differ from triangles or ellipses (even presenting regions that have a non-convex shape, but still connected).

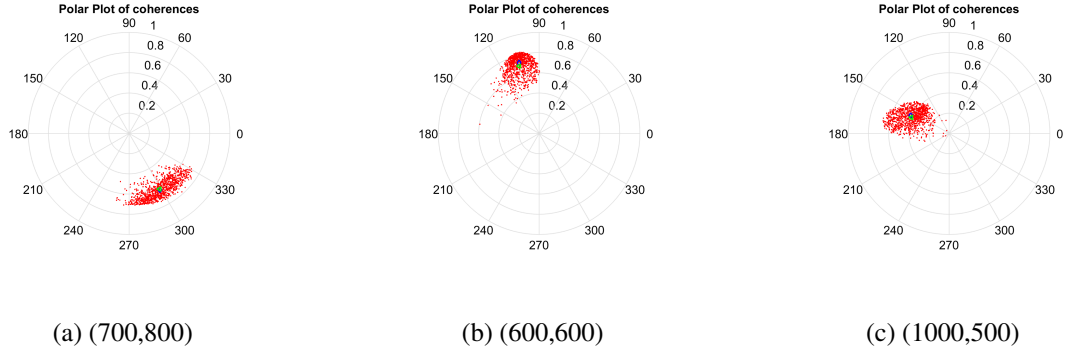


Fig. 18. AGRISAR dataset, L-band (E-SAR). Coherence loci for three generic points in the image. The pixel coordinates of the points are: (a) (700,800); (b) (600,600); (c)(1000,500). Pixel count starts from top left corner (Matlab convention) and the displayed images are 1500×2000 pixels. Red points: CoRe; Blue diamond: γ_{tr} ; Green triangle: Monte Carlo integral (MCI). Boxcar filter: 9×9 pixels.

515 The three previous examples show how γ_{tr} and MCI are very close. This example allows
 516 to formulate more on the idea of using γ_{Tr} in classification. If we observe the CoRe for point
 517 (a) ([700,800]) compared to point (b) ([600,600]) and (c) ([1000,500]), the size and shape of
 518 the region (a) appears to be difference from (b) and (c). This is because (a) represents winter
 519 wheat and (b) and (c) are two different fields of field grass. It is also apparent that there is
 520 some change in the distribution of the points for (b) and (c) which may be due to different
 521 grass height. To observe differences between shapes and distribution of points we could
 522 calculate the histograms of the CoRe points. This is a very slow procedure which can be
 523 highly inaccurate in the case of uniformly distributed points even if the bin size and number
 524 of points are properly selected. To avoid calculating histograms, we could investigate the
 525 point distribution using γ_{Tr} . For instance, we could observe the distance of the geometrical
 526 center of the CoRe (which could be calculated using the CoRe boundary) and comparing
 527 this to γ_{Tr} . Additionally, this distance, combined with other geometrical indicators (e.g. the
 528 ratio between the major and minor axis), could be included in a feature vector of a classifier
 529 to discriminate between different volume structures.

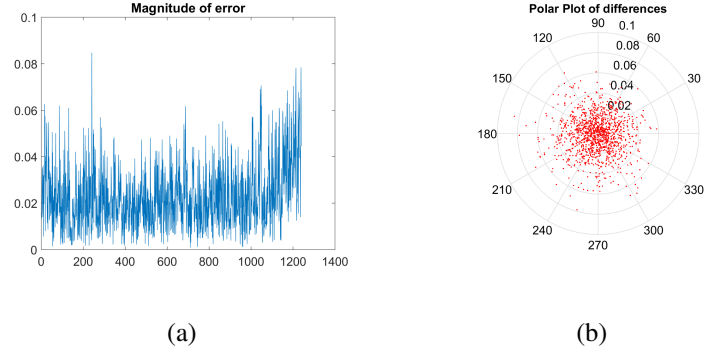


Fig. 19. AGRISAR dataset, L-band (E-SAR). (a) Difference between γ_{tr} and MCI; (b) Difference represented on polar plot

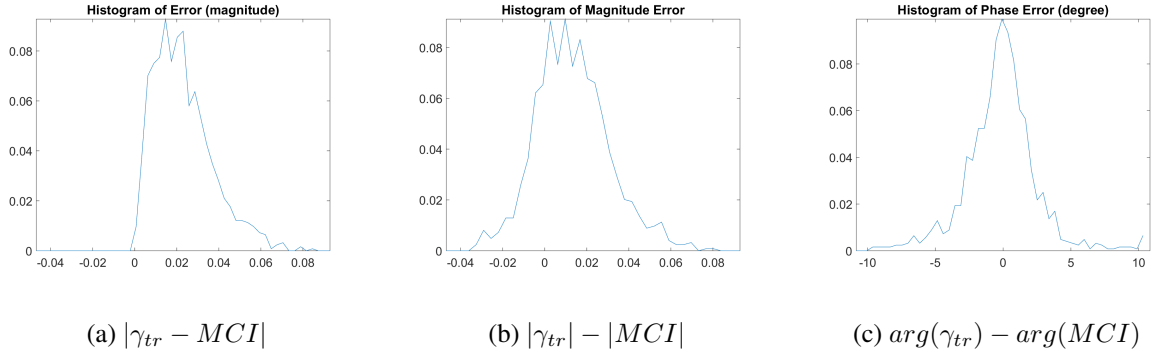


Fig. 20. AGRISAR dataset, L-band (E-SAR). Histograms of differences between γ_{tr} and MCI. (a) Magnitude of the error: $|\gamma_{tr} - MCI|$; (b) Difference of magnitudes: $|\gamma_{tr}| - |MCI|$; (c) Difference of phase: $\arg(\gamma_{tr}) - \arg(MCI)$ (in degrees).

In order to have a more quantitative comparison for the quality of the approximation the scene is sampled with a grid of 50 pixels width in range and azimuth and the resulting 1200 pixels are used to extract statistics. Figure 19.a presents the magnitude of the difference between γ_{tr} and MCI, while 19.b presents the same difference as complex numbers on a polar plot. Interestingly, the difference seems to be rather contained with values on average around 0.02. Moreover, the distribution of the errors on the polar plot is quite homogeneous which suggests that there are no biases.

To investigate these last points some histograms are shown in Figure 20. Additionally, Table II shows the mean and standard deviation associated with the distributions depicted by

TABLE II

MEAN AND STARNDARD DEVIATION (STD) OF ERROR.

	$ \gamma_{tr} - MCI $	$ \gamma_{tr} - MCI $	$arg(\gamma_{tr}) - arg(MCI)$ (degrees)
Mean (test 1)	0.023	0.013	-0.54
std (test 1)	0.013	0.017	2.13
Mean (test 2)	0.032	0.017	0.23
std (test 2)	0.017	0.023	7.00
Mean (test 3)	0.021	0.015	-0.80
std (test 3)	0.012	0.014	2.24

the histograms. The mean error is rather small and therefore it should affect only slightly the estimation of the center of mass. It is also interesting to note that the phase error is particularly small, with zero mean and a standard deviation of 2 degrees. It is important to keep in mind that the phase error (or ambiguity) introduced by the limited amount of samples (e.g. the Cramer Rao lower bound for the coherence phase) is expected to be higher than the approximation error.

To provide more quantitative data, two different acquisitions in the AGRISAR dataset are considered. These were acquired on the 19th of April and 21st of June. Also a different region of the dataset is examined. The larger time interval allows to evaluate lower values of coherence. Specifically, the average value of the magnitude of γ_{tr} over the area is around 0.26. The error increases slightly compared to the previous case, especially the standard deviation of the phase. A reason may be that the low coherence makes phase estimation challenging, since we are closer to zero (and the phase of zero is not defined). Please note such an issue affects strongly the MCI integral that would need more points to estimate the

553 phase properly. As a final test another combination of images is used considering the dates
 554 13st and 21st of June. The reduced time interval allows to have higher values of coherence.
 555 Now the average magnitude of γ_{tr} is 0.53. The improved value of coherence allows better
 556 estimations and reduces the error.

557 The final test concerns the estimation of the difference between the peak and γ_{tr} or MCI.
 558 Unfortunately, the analysis could not be accomplished successfully because we did not man-
 559 age to produce reliable estimates of the peak location. The plots for this analysis are not
 560 presented here because unreliable, however it is still possible to observe that γ_{tr} appears to
 561 be generally closer to the peak. As discussed previously the problem in estimating the peak
 562 is that the density can have rather small derivatives for values of entropy higher than 0.5 and
 563 a Monte Carlo search with histograms fails.

564 V. DISCUSSIONS AND CONCLUSIONS

565 The main goal of this paper was to propose a new operator for Polarimetric SAR Inter-
 566 ferometry (Pol-InSAR), namely the Trace Coherence γ_{tr} . This operator is an approximation
 567 of the center of mass of the coherence region (CoRe), that can be formally evaluated as the
 568 integral of the Pol-InSAR coherence γ over all the projection vectors.

569 The following mathematical proofs were given:

- 570 (1) The integral of a quadratic form is equal to the third part of its trace.
- 571 (2) The integral of γ is equal to the new operator Trace Coherence γ_{tr} in the following
 572 situations:
 - 573 (a) Polarimetric entropy equal to zero or one.
 - 574 (b) Polarimetric stationarity and single decorrelation process (i.e. all the scattering
 575 mechanisms have the same decorrelation and phase center).

576 The approximation was tested using Monte Carlo simulations and real data. γ_{tr} represents
 577 a good approximation in several situations. In particular, the error depends on the density of
 578 points in the CoRe. The accuracy of the approximation degrades as the CoRe size increases
 579 and the skewness of the CoRe increases. This is because γ_{tr} appears to be closer to the
 580 location of the density peak that can differ from the mean. As a consequence, γ_{tr} can also
 581 be used as an approximation of the peak location when this is very different from the mean.
 582 The latter is an interesting feature since it is particularly hard to retrieve the peak location
 583 when the polarimetric entropy is higher than 0.5.

584 The tests on real data (AGRISAR 2006, DLR) showed an average error of approximately
 585 0.025 in magnitude and less than 3 degrees in phase; however, the average phase error can
 586 increase to as much as 7 degrees for low values of coherence (around 0.2).

587 As a future work, a larger dataset with available ground measurements will be used to
 588 validate specific applications in the context of coherent change detection and classification.
 589 Specifically, a set of indexes will be designed and tested against different forest types to
 590 understand if different forest structures can be discriminated by this synthetic information.

591 APPENDIX

592 Here, the proof of the integral of a single quadratic form is equal to the third part of the
 593 matrix Trace is provided.

The integral can be rewritten as:

$$\begin{aligned} \frac{1}{S} \int_{\Theta} \underline{\omega}^{*T} T \underline{\omega} d\underline{\omega} &= \frac{1}{S} \int_{\Theta} \text{Trace} [\underline{\omega}^{*T} T \underline{\omega}] d\underline{\omega} \\ &= \text{Trace}[T] \frac{1}{S} \int_{\Theta} \text{Trace} [\hat{T} \Omega] d\underline{\omega}, \end{aligned} \quad (9)$$

594 where $\hat{T} = \frac{T}{\text{Trace}[T]}$ and $\Omega = \underline{\omega} \underline{\omega}^{*T}$. The latter passage was obtained calling the property of

595 cyclic permutation of the Trace (i.e. the first $\underline{\omega}$ is moved after the second $\underline{\omega}$).

In our case, T is Hermitian and therefore it can be diagonalized. Without loss of generality, we can use the eigenvector basis \underline{u}_i with $i = 1, 2, 3$ to represent any vector in the space. The integral variable $\underline{\omega}$ can be written as a linear combination of the eigenvector basis. Therefore,

$$\underline{\omega} = a\underline{u}_1 + b\underline{u}_2 + c\underline{u}_3, \quad (10)$$

$$|a|^2 + |b|^2 + |c|^2 = 1, \quad |a|^2 = A, \quad |b|^2 = B, \quad |c|^2 = C,$$

$$U_i = \underline{u}_i \underline{u}_i^{*T}.$$

It can be easily proven that the matrix Ω can be decomposed in the sum of three U_i matrices plus the sum of matrices with zero trace (i.e. in the eigenvector basis they only have off-diagonal elements). $\Omega = AU_1 + BU_2 + CU_3 + \sum_{\substack{i,j=1 \\ i \neq j}}^3 \sigma_{ij} U_{ij}$. Using the property of linearity of the Trace, the integral expression can be rewritten as:

$$\begin{aligned} \text{Trace}[T] \frac{1}{S} \int_{\Theta} \text{Trace} [\hat{T}\Omega] d\underline{\omega} = & \quad (11) \\ \text{Trace}[T] \frac{1}{S} \{ \text{Trace}[\hat{T}U_1] \int_{\Theta} A(\underline{\omega}) d\underline{\omega} + \text{Trace}[\hat{T}U_2] \int_{\Theta} B(\underline{\omega}) d\underline{\omega} + \text{Trace}[\hat{T}U_3] \int_{\Theta} C(\underline{\omega}) d\underline{\omega} \} = \\ \text{Trace}[T] \frac{1}{S} \{ \hat{\lambda}_1 \int_{\Theta} A(\underline{\omega}) d\underline{\omega} + \hat{\lambda}_2 \int_{\Theta} B(\underline{\omega}) d\underline{\omega} + \hat{\lambda}_3 \int_{\Theta} C(\underline{\omega}) d\underline{\omega} \} \end{aligned}$$

596 where $\hat{\lambda}_i$ are the eigenvalues divided by the sum of eigenvalues (i.e. the probability of the
597 eigenvalue). The last passage is possible because the off diagonal elements of T are zero in
598 the eigenvector basis. Therefore, the product with the matrices containing off-diagonal ele-
599 ments will return a matrix with only off-diagonal elements, which is traceless. $\text{Trace}[\hat{T}U_i]$
600 is a constant with respect to $\underline{\omega}$.

The three integrals are computed on the projections of the vector $\underline{\omega}$ over the eigenvector basis that varies when $\underline{\omega}$ is changed. Moreover, the three integrals have the same value, since each of the components will cover the same volume of space while $\underline{\omega}$ is swept over the entire

unitary complex sphere. Since they are squared values they vary inside a (non-negative) cube of unitary side. To conclude, the three integrals have to sum to one (i.e. the volume is unitary) and they have to be equal, therefore each of the integrals has to be equal to one third.

$$\begin{aligned} \text{Trace}[T] \frac{1}{3} [\text{Trace}(\hat{T}U_1 + \hat{T}U_2 + \hat{T}U_3)] &= \\ &= \text{Trace}[T] \frac{1}{3} (\text{Trace}[\hat{T}(U_1 + U_2 + U_3)]) = \text{Trace}[T] \frac{1}{3} \text{Trace}[\hat{T}I]. \end{aligned} \quad (12)$$

601 The sum of the three eigenvector matrices in the eigenvector basis is clearly the identity
602 matrix I (i.e. they are the standard basis), therefore the solution of the integral is:

$$\frac{1}{S} \int_{\Theta} \underline{\omega}^{*T} T \underline{\omega} d\omega = \frac{\text{Trace}(T)}{3} \quad (13)$$

603

ACKNOWLEDGEMENT

604 The AGRISAR2006 data were acquired by the E-SAR airborne system of DLR and they
605 were provide by ESA.

606 The author would like to thank Simon Zwieback (ETH Zurich) for the engaging conversa-
607 tions about potato-like shapes of coherence regions that helped the development of the ideas
608 in this work. The author would also like to thank Prof. Irena Hajnsek (ETH Zurich and DLR)
609 for the support of the work that was carried out at ETH Zurich.

610

REFERENCES

- 611 [1] G. Franceschetti and R. Lanari, *Synthetic Aperture Radar Processing*, CRC Press, 1999.
- 612 [2] I. H. Woodhouse, *Introduction to Microwave Remote Sensing*, CRC Press, 2004.
- 613 [3] S. R. Cloude, *Polarisation: Applications in Remote Sensing*, Oxford University Press, Oxford, UK, 2009.
- 614 [4] J. S. Lee and E. Pottier, *Polarimetric radar imaging: from basics to applications*, CRC Press, Taylor & Francis
615 Group, 2009.
- 616 [5] S.R. Cloude and K.P. Papathanassiou, "Polarimetric SAR interferometry," *IEEE Trans. on Geos. & Rem. Sen.*, vol.
617 36, no. 5, pp. 1551–1565, Sep. 1998.

- 618 [6] K. P. Papathanassiou and S. R. Cloude, "Single-baseline polarimetric SAR interferometry," *IEEE Trans. on Geos. &*
619 *Rem. Sens.*, vol. 39, pp. 2352–2363, 2001.
- 620 [7] S.R. Cloude and K.P. Papathanassiou, "Three-stage inversion process for polarimetric SAR interferometry," *IEE*
621 *Proceedings Radar, Sonar and Navigation*, vol. 150, no. 3, pp. 125 – 134, June 2003.
- 622 [8] D. Ballester-Berman, Lopez-Sanchez J. M., and J. Fortuny-Guasch, "Retrieval of biophysical parameters of agricul-
623 tural crops using polarimetric SAR interferometry," *IEEE Transactions on Geoscience and Remote Sensing*, vol. 43,
624 no. 4, Apr. 2005.
- 625 [9] S. Zwieback, S. Hensley, and I. Hajnsek, "A polarimetric first-order model of soil moisture effects on the DInSAR
626 coherence," *MDPI, Remote Sensing*, vol. 7, no. 6, pp. 7571–7596, June 2015.
- 627 [10] A. Marino, "A notch filter for ship detection with polarimetric SAR data," *IEEE Journal of Selected Topics in Applied*
628 *Earth Observations and Remote Sensing*, vol. 6, no. 3, pp. 1219 – 1232, June 2013.
- 629 [11] A. Marino, *A New Target Detector Based on Geometrical Perturbation Filters for Polarimetric Synthetic Aperture*
630 *Radar (POL-SAR)*, Springer-Verlag, 2012.
- 631 [12] S. R. Cloude and E. Pottier, "An entropy based classification scheme for land applications of polarimetric SAR,"
632 *IEEE Transactions on Geoscience and Remote Sensing*, vol. 35, pp. 68–78, 1997.
- 633 [13] A.P. Doulgeris, S.N. Anfinson, and T. Eltoft, "Classification with a non-Gaussian model for PolSAR data," *IEEE*
634 *Transactions on Geoscience and Remote Sensing*, vol. 46, no. 10, pp. 2999 – 3009, Oct. 2008.
- 635 [14] V. Carotenuto, A. De Maio, C. Clemente, and J. J. Soraghan, "Invariant rules for multipolarization SAR change
636 detection.," *IEEE Transactions on Geoscience and Remote Sensing*, vol. 53, no. 6, pp. 3294–3311, June 2015.
- 637 [15] K. Conradsen, A. A. Nielsen, J. Schou, and H. Skriver, "A test statistic in the complex Wishart distribution and its
638 application to change detection in polarimetric SAR data," *IEEE Trans. on Geos. & Rem. Sen.*, vol. 41, 2003.
- 639 [16] A. Marino, S. R. Cloude, and J. M. Lopez-Sanchez, "A new polarimetric change detector in radar imagery," *IEEE*
640 *Transactions on Gescience and Remote Sensing*, vol. 51, no. 5, pp. 2986 – 3000, 2013.
- 641 [17] A. Marino and I. Hajnsek, "A change detector based on an optimization with polarimetric SAR imagery," *IEEE*
642 *Transactions on Geoscience and Remote Sensing*, vol. 52, no. 8, pp. 4781–4798, Aug. 2014.
- 643 [18] S. R. Cloude and E. Pottier, "A review of target decomposition theorems in radar polarimetry," *IEEE Transactions on*
644 *Geoscience and Remote Sensing*, vol. 34, pp. 498–518, 1996.
- 645 [19] R. A. Horn and C. R. Johnson, *Topics in matrix analysis*, Cambridge University Press, 1991.
- 646 [20] G. Strang, *Linear Algebra and its Applications*, Thomson Learning, 1988.
- 647 [21] T. Flynn, M. Tabb, and R. Carande, "Coherence region shape extraction for vegetation parameter estimation in
648 polarimetric sar interferometry," *Proc. IGARSS, Toronto, ON, Canada, Jun.*, vol. 5, pp. 2596–2598, 2002.
- 649 [22] A. Marino and I. Hajnsek, "Linking the polarimetric change detector based on perturbation filters with the Pol-InSAR
650 coherence," *Proceedings on IGARSS12, 22-27 July, Munich*, 2012.

- [23] S. R. Cloude and K. P. Papathanassiou, "Polarimetric optimization in radar interferometry," *Electronics Letters*, vol. 33, no. 13, pp. 1176–1178, Jun. 1997.
- [24] M. Preiss and N. J. S. Stacy, "Coherent change detection: Theoretical description and experimental results," *Defence Science and Technology Organisation*, pp. 1–116, August 2006.
- [25] M. Weber, A. Marino, F. Kock, and I. Hajnsek, "Monitoring floods in the Kafue Flats with TanDEM-X data," *IEEE International Symposium on Geoscience and Remote Sensing IGARSS, Milan, Italy.*, pp. 1191 – 1194, 26-31 Jul 2015.
- [26] M. Neumann, L. Ferro-Famil, and A. Reigber, "Estimation of forest structure, ground, and canopy layer characteristics from multibaseline polarimetric interferometric SAR data," *IEEE Transaction on Geoscience and Remote Sensing*, vol. 48, no. 3, pp. 1086 –1104, Oct. 2010.
- [27] M. Pardini, A. Torano Caicoya, F. Kugler, S-K. Lee, I. Hajnsek, and K. Papathanassiou, "On the estimation of forest vertical structure from multibaseline polarimetric SAR data," *IEEE International Symposium Geoscience and Remote Sensing IGARSS, Munich.*, pp. 3443–3446, Jul. 2012.
- [28] A. Roueff, A. Arnaubec, P. Dubois-Fernandez, and P. Réfrégier, "Cramer-Rao Lower Bound analysis of vegetation height estimation with Random Volume Over Ground model and polarimetric SAR interferometry," *IEEE Geoscience and Remote Sensing Letter*, vol. 8, no. 6, pp. 1115–1119, 2011.
- [29] M. Laval, M. Simard, and S. Hensley, "A temporal decorrelation model for polarimetric radar interferometers," *IEEE Transactions on Geoscience and Remote Sensing*, vol. 50, no. 7, pp. 2880–2888, Jul 2012.
- [30] A. Touzi, R. and Lopes, J. Bruniquel, and P.W. Vachon, "Coherence estimation for SAR imagery," *IEEE Transactions on Geoscience and Remote Sensing*, vol. 37, no. 1, pp. 135–149, Jan. 1999.
- [31] A. Marino and I. Hajnsek, "Applications of integrals of quadratic forms for polarimetric sar data," *Proc. IGARSS, Milan, Italy.*, pp. 1–4, July 2015.
- [32] A. Marino and I. Hajnsek, "Solving the integral of quadratic forms of covariance matrices for applications in polarimetric radar imagery," *Proc. POLinSAR, Frascati, Italy*, January 2015.